Investigation of the space-variance effect in digital holography

XINGYU YANG,[1] ZIXIN ZHAO,[1,*] CHEN FAN,[1] YIJUN DU,[1] JUNXIANG LI,[1] GAOPENG ZHANG[2,*]

[1]*State Key Laboratory for Manufacturing Systems Engineering, School of Mechanical Engineering, Xi'an Jiaotong University, Xi'an, Shaanxi 710049, China*
[2]*Xi'an Institute of Optics and Precision Mechanics, Chinese Academy of Sciences, Xi'an, Shaanxi 710119, China*
*zixinzhao@xjtu.edu.cn
*zhanggaopeng@opt.ac.cn

Abstract: In classical Fourier optics, an optical imaging system is regarded as a linear space-invariant system which is only an approximation. Especially in digital holography, the space-variance effect has a great impact on the image quality and cannot be ignored. Therefore, it is comprehensively investigated in this article. Theoretical analyses indicate that, the space-variance effect is caused by linear frequency modulation and ideal low-pass filtering and it can be divided into three states: approximate space-invariance state, high-frequency distortion state, and boundary-diffraction state. Classical Fourier optics analysis of optical imaging systems only considers the first. Regarding the high-frequency distortion state, the closer the image field is to the edge, the more severe is the distortion of high-frequency information. As for the boundary-diffraction state, in addition to the distortion of high-frequency information in the margin, a prominent boundary-diffraction phenomenon is observed. If the space-variance effect of the imaging lens is ignored, we predict that no space-variance effect in image holography will occur when the hologram is recorded at the back focal plane of the imaging lens. Simulation and experimental result were presented to validate our theoretical prediction.

1. Introduction

In signal and systems theory, a system whose properties do not change with its spatial location is called a space-invariant system. In particular, the system response only depends on the input signal and the system characteristics, and is independent of the spatial location where the input signal is imposes. Due to the linear space invariance of optical imaging systems, classical Fourier optics describes the optical imaging system in terms of the frequency response from the perspective of signals and systems[1].

However, the space invariance of optical imaging systems is only a simplification. Related studies have pointed out that the space variance lowers the image quality of the part of the image field that is farther away from the optical axis. Accordingly, this simplification may be inappropriate for some cases. Yan et al.[2] discussed the axial measurement error caused by the space-variance effect in digital holography by performing numerous simulations of point and line spread functions. Lohmann and Paris[3] defined the cross-correlation of two-line spread functions in an optical system as the evaluation index of the space-variance effect of the system. Moreover, Brainis[4] investigated the space-variance effect in aperture and lens imaging by analyzing the point spread function.

The aforementioned articles research optical systems by analyzing the point spread function, which is classical in Fourier optics. The responses of any point or edge in a space-invariant system are the same, and every point or line is representative. A linear space-invariant system satisfies the convolution theorem and its transfer function can be

expressed by the Fourier transform of its point spread function. Therefore, point and edge spread functions can accurately describe the properties of space-invariant systems. However, no transfer function is present in the space-variant system, and the point spread function of a certain point can only describe the local response of the system to the point, which is unrepresentative. Therefore, it cannot holistically or comprehensively describe the system.

This study focuses on the causes of the space-variance effect, which have been studied by some scholars. Tichenor and Goodman[5] identified the quadratic phase factor as breaking the space-invariance condition of the single-lens imaging system. However, they only studied the conditions under which the quadratic phase factor can be ignored. Thus, although the optical imaging system can be simplified as a space-invariant system, the properties of the optical imaging system under space-variance effects cannot be analyzed. Pan et al.[6] showed that the spectrum broadening attributed to the quadratic phase factor was an important contribution to the space-variance effect, but their discussion on the space-variance effect was qualitative and not comprehensive. Herein, the role of the quadratic phase factor in the space-variance effect and its propagation law in digital holographic imaging systems are elucidated through a rigorous mathematical derivation.

Digital holography, an important three-dimensional measurement technology, can simultaneously record the intensity and phase information of the measured object. It is widely used in cell observation[7-9], particle and flow field measurement[10-12], topography[13-15] and tomography[7, 16, 17] measurement, among others. According to the space-invariance approximation criterion proposed by Tichenor and Goodman[5], the width of the object field of view(FOV) should be less than 1/4 of the width of the aperture. This is easy to achieve for lens imaging. However, due to the limitation of resolution and magnification in digital holography, the transverse size of the object under test or the virtual image of the front imaging system is usually comparable to the size of the CCD/CMOS chip, so the space-variance effect is very common in digital holography, especially digital Fresnel holography[18-21].

This paper analyzes the mathematical model of the Fresnel holographic imaging system, and determines that the image field is not the result of the ideal low-pass filtering of the object field, as described in the classical Fourier optics, but the result of the object field first modulated by the linear frequency modulation (LFM) signal and then filtered by the ideal low-pass filter. Thereafter, according to the ratio of the space-bandwidth product between the LFM signal and the aperture, the space-variance effect of the holographic imaging system is categorized as approximate space invariance, high-frequency distortion, and boundary diffraction states. Notably, the classical Fourier optical analysis of optical imaging systems only considers the approximate space-invariance state, which can be reduced to a space-invariant system. In the high-frequency distortion state, the closer the image field is to the FOV edge, the more severe the high-frequency information distortion is. In the boundary-diffraction state, in addition to the distortion of high-frequency information in the FOV margin, boundary-diffraction fringes are prominent. Specifically, the Fresnel diffraction pattern of the aperture stop can be observed on the image field. To validate our theory, we predict that no space-variance effect occurs in the image holography[22, 23] when the hologram is recorded in the back focal plane of the imaging lens if the space-variance effect of the imaging lens is ignored. Simulations and experiments are conducted to confirm this prediction. For simplicity, the theoretical derivation in this paper is based on the one-dimensional imaging case, but it can be easily extended to the two-dimensional case.

The rest of this article is organized as follows. In Section 2, the mathematical model of Fresnel holography with considering space-variance effect is established. In Section 3, the space-variance effect is divided into three states. In Section 4, the prediction is proposed and confirmed by simulations and experiments.

2. Mathematical model of space-variant Fresnel holographic imaging systems

Diffraction in the free space is linear space-invariant. According to the Huygens–Fresnel principle, "*every unobstructed point of a wavefront, at a given instant, serves as a source of spherical quadratic wavelets. The amplitude of the optical field at any point beyond is the superposition of all these wavelets.*[24]" The Huygens–Fresnel principle comprises two elements: spherical wavelets hypothesis and the combination mode of spherical wavelets—interference superposition. If the free-space diffraction is considered, the above points, respectively, correspond to the space-invariant and linear characteristics of free-space diffraction. If a system is linear space-invariant, it can be described by a transfer function. The free-space diffraction can be expressed by angular spectrum transfer function, as shown in Eq.(1):

$$H(f_x, f_y) = \begin{cases} exp[j\frac{2\pi z}{\lambda}\sqrt{1-(\lambda f_x)^2-(\lambda f_y)^2}], & {f_x}^2+{f_y}^2<\frac{1}{\lambda^2} \\ 0, \quad else \end{cases} \tag{1}$$

where

$$\begin{cases} f_x = \frac{cos\alpha}{\lambda} \\ f_y = \frac{cos\beta}{\lambda} \end{cases} \tag{2}$$

where α and β are the angles between the propagation direction and coordinate axes x and y, respectively, and λ is the wavelength.

However, although the diffraction limited optical system is linear, it is not space invariant[3, 25]. Without loss of generality, only one-dimensional imaging process is considered. Taking holography as an example, Fig.1 shows the recording and reconstruction process of Fresnel holography, where R is the reference wave. For simplicity, the back propagation is represented to the right. Planes x_0, x_1, and x_2 represent the object plane, CMOS target plane (or hologram plane), and observation planes, respectively.

In the case of one-dimensional imaging process, the spatial frequency satisfies the following equation:

$$f_x = \frac{\sqrt{1-cos^2\gamma}}{\lambda} = \frac{sin\gamma}{\lambda} \tag{3}$$

where γ is the angle between the propagation direction and coordinate axis z.

Diffraction in free space occurs from the object plane to CMOS target plane, but due to the finite aperture, the CMOS will only selectively receive the frequency components of each object point. For example, points A and B are located on the upper and lower sides of the optical axis, respectively, of the object plane. Eq.(3) indicates that because $\gamma_{A1} \neq \gamma_{B1}$ and $\gamma_{A2} \neq \gamma_{B2}$, the frequency components of A and B recorded by the CMOS are different, and the response on the observation plane markedly differs. Therefore, the diffraction limited optical system is space-variant system.

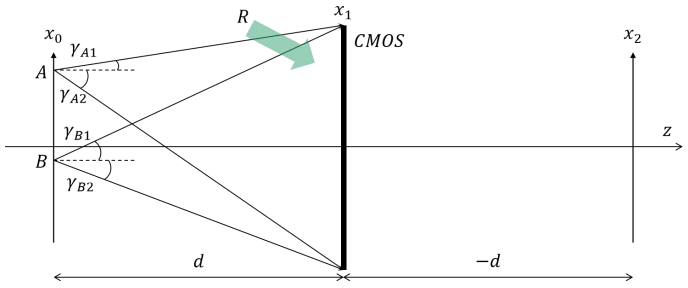

Fig. 1. the recording and reconstruction process of Fresnel holography

Considering the object field $u_o(x_o)$, diffraction from the object plane to the hologram plane is expressed using the Fresnel diffraction formula as follows:

$$u_1(x_1) = \frac{exp(jkd)}{j\lambda d} \int_{-\infty}^{\infty} u_0(x_0) w_0(x_0) exp\left[\frac{jk}{2d}(x_1 - x_0)^2\right] dx_0 \quad \textbf{(4)}$$

where d is the recording distance, $-d$ is the reconstruction distance, and $k = 2\pi/\lambda$. If the object field has a rectangular boundary and the side length is L_0, then $w_0(x_0) = rect\left(\frac{x_0}{L_0}\right)$, where $rect(\cdot)$ represents the rectangular window function. Let the reference wave be

$$R(x_1) = a_r exp[j\psi(x_1)] \quad \textbf{(5)}$$

The hologram can then be obtained from the interference between the object wave and the reference wave:

$$I_1(x_1) = |u_1(x_1) + R(x_1)|^2 = |u_1|^2 + |R|^2 + R^* u_1 + R u_1^* \quad \textbf{(6)}$$

By phase-shifting or applying the off-axis technique, the object wave u_1 recorded by the hologram can be extracted. Through back propagation, the reconstructed wave front $u_2(x_2)$ can be written as

$$\begin{aligned} u_2(x_2) = \frac{{a_r}^2}{\lambda^2 d^2} \int_{-\infty}^{\infty} w_1(x_1) \left\{ \int_{-\infty}^{\infty} u_0(x_0) rect\left(\frac{x_0}{L_0}\right) exp\left[\frac{jk}{2d}(x_1 - x_0)^2\right] dx_0 \right\} \\ \times exp\left[\frac{-jk}{2d}(x_2 - x_1)^2\right] dx_1 \end{aligned} \quad \textbf{(7)}$$

where $w_1(x_1)$ is the rectangular window function determined by the size of the CMOS chip, which can be regarded as the aperture stop of the Fresnel holographic imaging system. Ignoring the constant term in Eq.(7), we can derive the reconstructed wave front $u_2(x_2)$ as

$$\begin{aligned} & u_2(x_2) \\ & = exp\left(\frac{-jk}{2d}{x_2}^2\right) \\ & \times FFT^{-1}\left\{ rect\left(\frac{f_x}{L_1/\lambda d}\right) FFT\left[u_0(x_0) rect\left(\frac{x_0}{L_0}\right) exp\left(\frac{jk}{2d}{x_0}^2\right)\right]_{f_{x0}=\frac{x_1}{\lambda d}} \right\}_{t_{fx0}=x_0=x_2} \end{aligned} \quad \textbf{(8)}$$

where L_1 is the physical size of CMOS chip; FFT and FFT^{-1} represent the Fourier transform and inverse Fourier transform, respectively; f_{x0} is the frequency domain coordinates after Fourier transform; and t_{fx0} is the spatial domain coordinates after inverse Fourier transform.

The system represented by Eq.(8) is shown in Fig. 2 as a block diagram. According to the communication theory, the input signal, namely the object field $u_0(x_0) rect\left(\frac{x_0}{L_0}\right)$, is the modulation signal, and its spectrum distribution in phase space is shown in Fig. 3(a) [26, 27]. $exp\left(\frac{jk}{2d}{x_0}^2\right)$ is the carrier signal, which is also called LFM signal or chirp signal. $u_0(x_0) rect\left(\frac{x_0}{L_0}\right) exp\left(\frac{jk}{2d}{x_0}^2\right)$ is the modulated signal. Fresnel holographic imaging system consists of the following three parts:

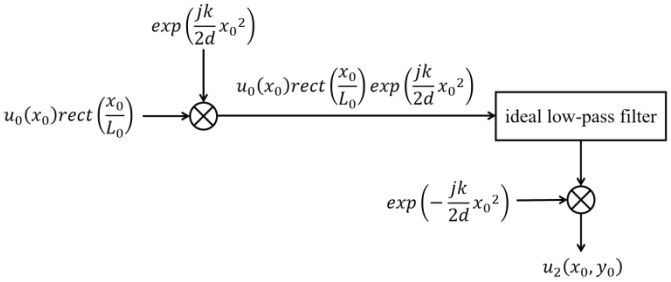

Fig. 2. block diagram of Fresnel holographic imaging system

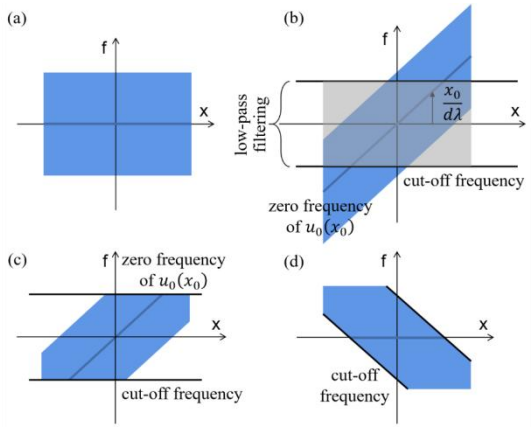

Fig. 3. Distribution of spectrum in phase space for each step in Fig.2. The f axis is the frequency, and the x axis is the spatial coordinate. (a) The spectrum distribution of object field $u_0(x_0)rect\left(\frac{x_0}{L_0}\right)$ in phase space. The thick blue line is the zero-frequency component of object field $u_0(x_0)rect\left(\frac{x_0}{L_0}\right)$. (b) The spectrum distribution of the modulated signal $u_0(x_0)rect\left(\frac{x_0}{L_0}\right)exp\left(\frac{jk}{2d}x_0^2\right)$ in phase space, which can be obtained by shearing (a) by $\frac{x_0}{d\lambda}$. The thick black line is the cut-off frequency. (c) Distribution of spectrum in phase space after ideal low-pass filtering. (d) The spectrum distribution of the reconstructed wave field $u_2(x_2)$ in phase space, which can be obtained by shearing (c) by $-\frac{x_0}{d\lambda}$.

(1)Modulation of input signal $u_0(x_0)rect\left(\frac{x_0}{L_0}\right)$ by carrier signal $exp\left(\frac{jk}{2d}x_0^2\right)$. If $\varphi = \frac{k}{2d}x_0^2$, the frequency shift introduced by carrier signal $exp\left(\frac{jk}{2d}x_0^2\right)$ when applying the frequency shift theorem of Fourier transform is

$$\Delta f_x = \frac{1}{2\pi}\cdot\frac{\partial\varphi}{\partial x_0} = \frac{x_0}{d\lambda} \tag{9}$$

Eq.(9) shows that the frequency shift is dependent on the spatial coordinates, which indicates that this process is space-variant. The distribution of modulated signal $u_0(x_0)rect\left(\frac{x_0}{L_0}\right)exp\left(\frac{jk}{2d}x_0^2\right)$ in phase space is shown in Fig. 3(b).

(2)Ideal low-pass filtering of modulated signal $u_0(x_0)rect\left(\frac{x_0}{L_0}\right)exp\left(\frac{jk}{2d}x_0^2\right)$. $rect\left(\frac{f_x}{L_1/\lambda d}\right)$ represents a rectangular ideal low-pass filter, as shown in Fig. 4, whose passband is determined by the angular aperture of the CMOS target plane, namely $-\frac{L_1}{2\lambda d} \leq f_x \leq \frac{L_1}{2\lambda d}$. As shown in Fig. 3(b) and Fig.3(c), after the frequency shift of the modulation signal, the original low-frequency information becomes high-frequency. In this case, low-pass filtering will block the original low-frequency information of the modulation signal

$u_0(x_0)rect\left(\frac{x_0}{L_0}\right)$. The farther away it is from the optical axis, the more low-frequency information of the modulation signal $u_0(x_0)rect\left(\frac{x_0}{L_0}\right)$ will be lost. Therefore, for the input signal of the system–object field $u_0(x_0)rect\left(\frac{x_0}{L_0}\right)$, the aperture is not reflected as an ideal low-pass filter due to the frequency shift effect of Eq.(9), but as a frequency selective filter with constant passband width and center frequency changing with the position in object plane. Such a filter presents different frequency responses with different spatial locations of the modulation signal $u_0(x_0)rect\left(\frac{x_0}{L_0}\right)$; that is, the filtering process is space-variant for the modulation signal $u_0(x_0)rect\left(\frac{x_0}{L_0}\right)$.

(3)Modulation of ideal low-pass filtered signal by carrier signal $exp\left(-\frac{jk}{2d}{x_0}^2\right)$. When the reconstruction distance is equal to the recording distance, the two carrier signals before and after filtering are conjugate and cancel each other, and the Fresnel holography reconstruction automatically completes the demodulation process. Therefore, the problem of quadratic phase aberration is not encountered in Fresnel holography. The distribution of the reconstructed wave field in phase space is shown in Fig. 3(d).

The above analyses reveal that LFM and ideal low-pass filtering are critical to the space-variance effect. Without LFM, the ideal low-pass filtering is strict with respect to the object field, and the system will be space-invariant. Moreover, without ideal low-pass filtering, the two carriers will cancel out, and the reconstructed wave front will not differ from the object wave field.

3. Three stages of the space-variance effect

The solution to Eq.(8) is derived to further analyze the space-variance effect. From the perspective of signal processing, the chirp rate of the LFM signal $exp\left(\frac{jk}{2d}{x_0}^2\right)$ is $K_0 = 1/d\lambda$, its bandwidth is $B_0 = K_0L_0$, and its space bandwidth product is $SBP_0 = B_0L_0 = K_0{L_0}^2$. The object wave field $u_0(x_0)$ is assumed to be a slowly varying function compared with the LFM signal $exp\left(\frac{jk}{2d}{x_0}^2\right)$; therefore, it can be ignored. This approximation is reasonable for phase-only samples with slow phase changes, such as cells. The modulated signal can be reduced to $rect\left(\frac{x_0}{L_0}\right)exp(j\pi K_0{x_0}^2)$, and its Fourier transform is

$$\begin{aligned} U(f_{x_0}) &= \int_{-L_0/2}^{L_0/2} exp\left[j\pi\left(K_0{x_0}^2 - 2f_{x_0}x_0\right)\right]dx_0 \\ &= exp\left(-j\pi\frac{{f_{x_0}}^2}{K_0}\right)\int_{-L_0/2}^{L_0/2} exp\left[j\pi\left(\sqrt{K_0}x_0 - \frac{f_{x_0}}{\sqrt{K_0}}\right)^2\right]dx_0 \end{aligned} \quad (10)$$

Assume that $\left(\sqrt{K_f}f - \frac{x}{\sqrt{K_f}}\right)^2 = v^2/2,\ v = \sqrt{2K_0}x_0 - \frac{\sqrt{2}f_{x_0}}{\sqrt{K_0}}$, we have

$$U(f_{x_0}) = \frac{1}{\sqrt{2K_0}}exp\left(-j\frac{\pi{f_{x_0}}^2}{K_0}\right)\int_{-V_1}^{V_2} exp\left(j\frac{\pi v^2}{2}\right)dv \quad (11)$$

The integral term of Eq.(10) is the Fresnel integral, where

$$V_1 = \frac{\sqrt{2K_0{L_0}^2}}{2} + \sqrt{2/K_0}f_{x_0} \quad (12)$$

$$V_2 = \frac{\sqrt{2K_0{L_0}^2}}{2} - \sqrt{2/K_0} f_{x_0}$$

The the spectrum $U(f_{x_0})$ of signal $rect\left(\frac{x_0}{L_0}\right) exp(j\pi K_0 {x_0}^2)$ is then

$$U(f_{x_0}) = \frac{1}{\sqrt{2K_0}} exp\left(-j\pi \frac{{f_{x_0}}^2}{K_0}\right)[C(V_1) + jS(V_1) + C(V_2) + jS(V_2)] \quad \textbf{(13)}$$

where

$$C(V) = \int_0^V cos\left(\frac{\pi v^2}{2}\right) dv$$
$$S(V) = \int_0^V sin\left(\frac{\pi v^2}{2}\right) dv \quad \textbf{(14)}$$

As shown in Fig. (4), the red line is the magnitude spectrum of $U(f_{x_0})$ with rectangular envelope, and its main energy is relatively evenly distributed between $-\frac{B_0}{2}$ and $\frac{B_0}{2}$, rather than concentrated near the zero frequency such as in the classical distribution of the magnitude spectrum [28]. This phenomenon is called central frequency spreading[29, 30]. Eq.(13) offers a good approximation of the spectrum of the modulated signal $u_0(x_0) rect\left(\frac{x_0}{L_0}\right) exp\left(\frac{jk}{2d}{x_0}^2\right)$. Notably, the spectrum $U(f_{x_0})$ is only meaningful in the system represented in Eq.(8) or Fig. 2, and is independent of the object wave $u_1(x_1)$ recorded by the hologram.

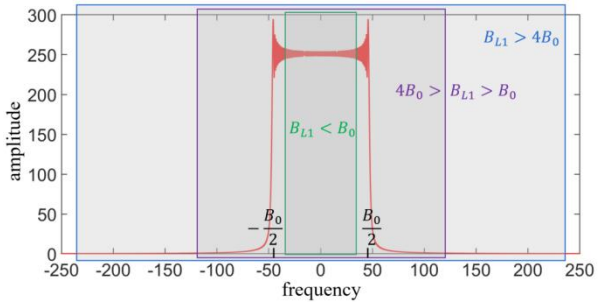

Fig. 4 schematic of the amplitude spectrum of spectrum $U(f_{x_0})$

The low-pass filtering process can be divided into three states.

(1)Approximate space-invariance state. In this state, the filter passband width $B_{L1} = L_1/\lambda d$ is much larger than the bandwidth $B_0 = L_0/d\lambda$ of the LFM signal, that is, the width of aperture L_1 is much larger than the width of the object field L_0. The blue box in Fig.4 represents the passband of the low-pass filter in this case. Tichenor and Goodman[5] pointed out that when $L_1 > 4L_0$, the space-variance effect is negligible. The classical Fourier optical analysis of the optical imaging systems rests on the assumption of approximate space invariance; in other words, only the $L_1 > 4L_0$ case is considered.

(2)High-frequency distortion state. The passband width of the filter in this state satisfies $4B_0 > B_{L1} > B_0$. The purple box in Fig. 4 represents the passband of the low-pass filter in this case. The energy blocked by the filter is mainly from the high-frequency information of the object field far from the optical axis. The farther away the object wave field is from the optical axis, the higher is the frequency modulated by the LFM signal. Therefore, more information is lost in these areas after low-pass filtering, and the image quality is worse,

which is mainly reflected in the distortion of the abrupt phase in the margin of the image wave field.

(3)boundary-diffraction state. The green box in Fig. 4 represents the passband of the low-pass filter when $B_{L1} < B_0$. In this case, the high-frequency and a mass of low-frequency information in the margin of the object wave field are filtered out. Because the main energy of the optical field is concentrated in the low-frequency information, high energy loss occurs in areas where low-frequency information is filtered out, which leads to a decrease in the signal-to-noise ratio, resulting in phase distortion.

When the space-bandwidth product $TBP = K_0{L_0}^2$ of LFM signal $exp(j\pi K_0{x_0}^2)$ is sufficiently large, the $U(f_{x_0})$ spectrum can be approximated as

$$U(f_{x_0}) = \frac{1}{\sqrt{K_0}} exp\left(-j\pi \frac{{f_{x_0}}^2}{K_0} + \frac{\pi}{4}\right), \quad -\frac{B_0}{2} < f_{x_0} < \frac{B_0}{2} \tag{15}$$

Eq.(15) demonstrates that the spectrum of the band-limited LFM signal can still be regarded as a band-limited LFM signal. Curlander and McDonough[31] pointed out that when the spatial bandwidth product of the LFM signal is greater than 100, Eq.(15) is sufficient for obtaining the exact spectrum. Therefore, when the filter passband width $B_{L1} = L_1/\lambda d$ is less than the bandwidth $B_0 = L_0/d\lambda$ of the LFM signal, that is, the aperture width L_1 is less than the object wave field width L_0, ignoring the constant phase, the spectrum after ideal low-pass filtering can be approximated as

$$U(f_{x_0}) = \frac{1}{\sqrt{K_0}} exp\left(-j\pi \frac{{f_{x_0}}^2}{K_0}\right), \quad -\frac{B_{L1}}{2} < f_{x_0} < \frac{B_{L1}}{2} \tag{16}$$

The signal presented in Eq.(16) is considered a new LFM signal. Let $K_1 = 1/K_0 = d\lambda$; its chirp rate is $-K_1$. The bandwidth $B_1 = K_1 B_{L1} = L_1$ is the physical width of the aperture. The space bandwidth product is $SBP_1 = K_1 {B_{L1}}^2 = \frac{{L_1}^2}{\lambda d}$, which is the same form as Fresnel number.

The inverse Fourier transform of $U(f_{x_0})$ is

$$\tilde{u}_2(x_2) = \frac{1}{\sqrt{K_0}} \int_{-B_{L1}/2}^{B_{L1}/2} exp\left[j\pi\left(-K_1 {f_{x_0}}^2 + 2f_{x_0}x_2\right)\right] df_{x_0} \tag{17}$$

From the derivation in Eq.(10)–Eq.(14), we can obtain

$$\tilde{u}_2(x_2) = \frac{1}{\sqrt{2}} exp\left(j\frac{\pi {x_2}^2}{K_1}\right)[C(X_1) - jS(X_1) + C(X_2) - jS(X_2)] \tag{18}$$

where

$$\begin{aligned} X_1 &= \frac{\sqrt{2K_1 {B_{L1}}^2}}{2} + \sqrt{2/K_1}x_2 = \sqrt{2N_{F1}}(1 + 2x_2/L_1) \\ X_2 &= \frac{\sqrt{2K_1 {B_{L1}}^2}}{2} - \sqrt{2/K_1}x_2 = \sqrt{2N_{F1}}(1 - 2x_2/L_1) \end{aligned} \tag{19}$$

where $N_{F1} = \frac{{L_1}^2}{4d\lambda}$. Substituting Eq.(18) into Eq.(8), the quadratic phase factor in Eq.(18) can be cancelled. The reconstructed wave front is

$$u_2(x_2) = \frac{1}{\sqrt{2}}[C(X_1) - jS(X_1) + C(X_2) - jS(X_2)] \tag{20}$$

which proves that no quadratic phase aberration is present in the Fresnel holography reconstructed wave front. The above derivation assumes that the object field changes slowly, so the solution to Eq. (20) can also be regarded as the wavefront error, which is caused by the space-variance effect on the low frequency of the image field.

Equation (20) is obtained from the back propagation of R^*u_1. The corresponding wavefront error $u_2(x_2)$ obtained from the forward propagation of R^*u_1 is

$$u_2(x_2) = \frac{1}{\sqrt{2}}[C(X_1) + jS(X_1) + C(X_2) + jS(X_2)] \quad \textbf{(21)}$$

Eq.(21) is exactly the same as the Fresnel diffraction pattern of the square aperture in [32]. The square aperture here is the CMOS chip. Therefore, $B_{L1} < B_0$ is an instance of the boundary-diffraction state. Moreover, Eq.(20) and Eq.(21) reveal that the boundary diffraction will disturb the entire image wave field, including the paraxial state.

Experimental results of the three stages of space-variance effect are shown in Fig. 5. The sample is a laser etched "XJTU" quartz plate with a maximum width of about 3 mm. The size of CMOS chip used in the experiment is 12.8 × 12.8 mm^2 (resolution 5120 × 5120, pixel size 2.5 × 2.5 μm^2). Therefore, if the object wave field of the measured sample is exactly located in the center of the CMOS chip, the approximate space-invariance state $L_1 > 4L_0$ is satisfied, as shown in Fig. 5 (a). In order to compare the measurement results of the same location of the same sample under different conditions, the sample is moved so that the relative position of the CMOS chip and the object wave field changes, which is equivalent to using a sample with larger size. If part of the main energy of the object wave field irradiates outside the CMOS chip, the boundary diffraction state $B_{L1} < B_0$ or $L_1 < L_0$ is satisfied, as shown in Fig. 5 (c). The condition between the cases shown in Fig. 5 (a) and Fig. 5 (c) corresponds to the high-frequency distortion state, as shown in Fig. 5 (b).

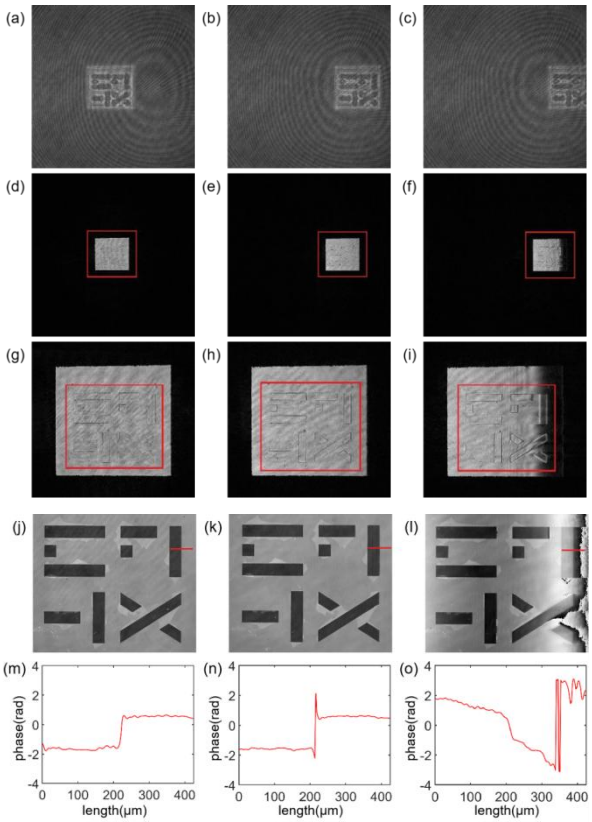

Fig. 5 Fresnel holographic measurements in the three stages of space-variance effect. (a–c) are Fresnel holograms recorded under three conditions: the diffraction wave field of the measured object falling on the center of the CMOS target plane, to the right but the main part is still on the CMOS target plane, and part of the direct light does not falling on the CMOS target plane. (d–f) represent the reconstructed intensity map of the three aforementioned

holograms, and zero padding to 7500×7500 pixels during reconstruction. (g–i) is the enlarged view of the red box area in (d–f). Distinct boundary diffraction fringes or ringing artifacts are evident in (i). (j–l) is the phase diagram corresponding to the red box area in (g–i). (m–o) is the contour line at the red line in figure (j–l). (n) shows the phase distortion at the step, which is caused by the loss of high-frequency information here due to the space-variance effect. (o) shows the perturbation of the low-frequency information by boundary-diffraction, and the overall trend of the contour is severely affected.

From the perspective of signal processing, this boundary-diffraction disturbance can be considered a ringing artifact, namely Gibb's phenomenon[6]. Cuche et al.[33] utilized the apodization method to suppress the boundary diffraction disturbance in digital holographic imaging and achieved good results in the application of holographic measurements[34]. In general, in addition to consuming more time and computational resources, and a reduced FOV, the apodization method can satisfactorily suppress the boundary diffraction perturbation of the intensity map. However, the apodization method does not fundamentally change the space-variance effect of the optical imaging system, so it cannot suppress the high-frequency information distortion in the marginal area of the reconstructed image. In addition, because the apodization method reduces the intensity of the hologram marginal area, the signal-to-noise ratio of the reconstructed image in the corresponding area decreases, which leads to more severe distortion of the phase map.

4. Eliminating the space-variance effect by recording holograms at the back focal plane of imaging lens

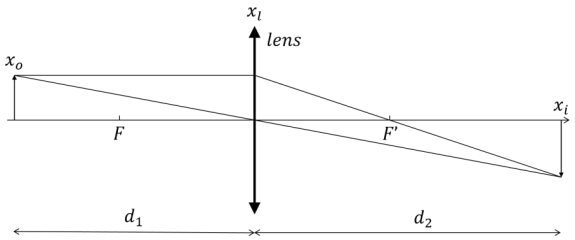

Fig. 6 Schematic of single-lens imaging. d_1 and d_2 are object and image distances, respectively; F and F' are focal points; and x_o, x_l, and x_i are coordinates of the object, lens and image plane, respectively

Due to the size of a CMOS chip, the numerical aperture of Fresnel holographic imaging system is usually much smaller than that of a lens imaging system. Moreover, increasing the numerical aperture by increasing the CMOS chip size is expensive and inefficient. Image holography[22, 23] is a hologram recording method that combines holography with lens imaging system. We deductively predict that hologram recording at the back focal plane of the imaging lens will not produce space-variance effect, and this prediction is proved by simulation and experiment. If the constant term is ignored, the expression of single-lens imaging is

$$u_i(x_i) = exp\left(\frac{jk}{2d_2}{x_i}^2\right) \times FFT^{-1}\left\{FFT\left[u_o(x_o)exp\left(\frac{jk}{2d_1}{x_o}^2\right)\right]_{f_{xo}=\frac{x_l}{\lambda d_1}} \times P(f_{xo})\right\}_{t_{fxo}=x_o=\frac{-d_1}{d_2}x_i} \tag{22}$$

where $P(\cdot)$ is the pupil function, and

$$\frac{1}{d_1}+\frac{1}{d_2}=\frac{1}{f} \tag{23}$$

where f is the focal length of the lens.

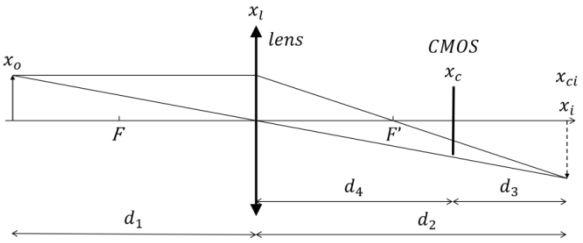

Fig. 7 Schematic of image holography. d_1 and d_2 are the object and image distances of the lens, respectively. The CMOS is located between the lens and the image plane, d_3 is the distance between the CMOS and the image plane, and d_4 is the distance between the lens and CMOS. F and F' are the front and back focal points of the lens, respectively. x_o, x_l, and x_i are the lens object, lens, and lens image planes, respectively. x_i is also the object plane of the holographic imaging system, which can be regarded as the virtual object. x_c and x_{ci} are the CMOS and reconstructed image planes, respectively. In this case, x_c lies between x_l and x_{ci}, and x_{ci} coincides with x_i.

In the image holography schematic shown in Fig. 7, the image holography consists of single-lens imaging and Fresnel holography when the diffraction between each plane is located in the Fresnel diffraction region. The image formed by the lens can be regarded as the virtual object in Fresnel holography. The recording distance is $-d_3$, and the reconstruction distance is d_3, with their signs being opposite to those in ordinary Fresnel holography. In this case, the formula for Fresnel holographic imaging is as follows

$$\begin{aligned} u_{ci}(x_{ci}) = & exp\left(\frac{jk}{2d_3}{x_{ci}}^2\right) \\ & \times FFT^{-1}\left\{FFT\left[u_i(x_i)exp\left(\frac{-jk}{2d_3}{x_i}^2\right)\right]_{f_{xi}=\frac{-x_c}{\lambda d_3}}\right. \\ & \left.\times rect\left(\frac{f_{xi}}{L_x/\lambda d_3}\right)\right\}_{t_{fxi}=x_i=-x_{ci}} \end{aligned} \tag{24}$$

Substituting Eq.(22) into Eq.(24) yields a cumbersome expression.

$$\begin{aligned} u_{ci}(x_{ci}) = & exp\left(\frac{jk}{2d_3}{x_{ci}}^2\right) \\ & \times FFT^{-1}\left\{FFT\left\{exp\left(\frac{jk}{2d_2}{x_i}^2\right)\right.\right. \\ & \times FFT^{-1}\left\{FFT\left[u_o(x_o)exp\left(\frac{jk}{2d_1}{x_o}^2\right)\right]_{f_{xo}=\frac{x_l}{\lambda d_1}}\right. \\ & \left.\left.\times P(f_{xo})\right\}_{t_{fxo}=x_o=\frac{-d_1}{d_2}x_i} \times exp\left(\frac{-jk}{2d_3}{x_i}^2\right)\right\}_{f_{xi}=\frac{-x_c}{\lambda d_3}} \\ & \left.\times rect\left(\frac{f_{xi}}{L_x/\lambda d_3}\right)\right\}_{t_{fxi}=x_i=-x_{ci}} \end{aligned} \tag{25}$$

As shown in Fig.8, the optical imaging system presented in Eq.(25) can be represented by a block diagram, and the former is analyzed in the phase space, as shown in Fig. 9. The modulation of the LFM signal in phase space is manifested as the shearing of the original signal, and the low-pass filtering is manifested as the cutting of the spectrum along the frequency axis. Because shearing occurs before cutting, different states retain different frequency components after cutting, as shown in Fig. 9(b), which will lead to space-variance effect. In Fig. 7, the virtual object field of holography is the image of the previous lens, which results in the spectrum undergoing reverse shearing and makes it possible to “correct” the spectrum before passing through the next low-pass filter, the CMOS, as shown in Fig. 9(d). In

this case, the frequency response of the CMOS low-pass filter to each spatial position is the same, and no new space-variance effect would be produced.

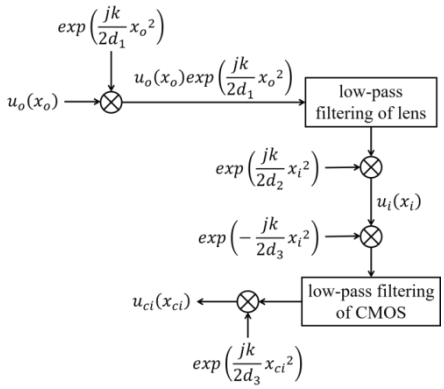

Fig. 8. Block diagram of the image holographic system shown in Fig.7 and Eq.(25)

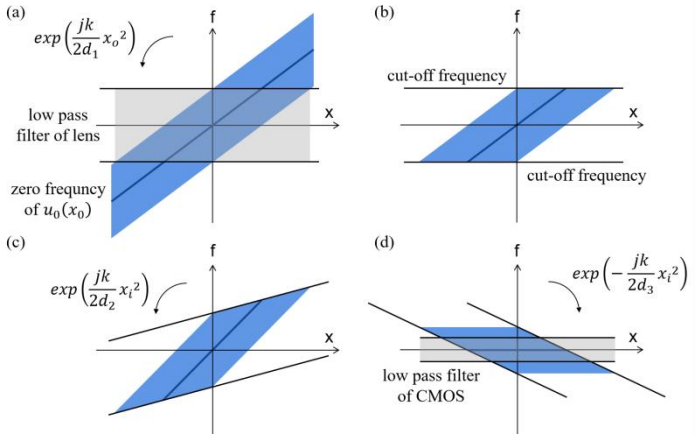

Fig. 9. Distribution of the spectrum in the phase space for each step in Fig.8. The f axis is the frequency, and the x axis is the spatial coordinate. The thick blue line represents the zero-frequency component of the object field $u_o(x_o)rect\left(\frac{x_0}{L_0}\right)$. (a) The modulation of the object field by the LFM signal is represented by shearing (rather than rotation) in the upper right and lower left or counterclockwise direction, after which the original low-frequency component linearly spreads to the high-frequency. (b) The result of low-pass filtering of modulated signal $u_o(x_o)rect\left(\frac{x_0}{L_0}\right)exp\left(\frac{jk}{2d_1}x_o^2\right)$. (c) Further modulation by the LFM signal $exp\left(\frac{jk}{2d_2}x_i^2\right)$. (d) The modulation effect of the LFM signal $exp\left(\frac{-jk}{2d_3}x_i^2\right)$ is represented by the upper left and lower right or clockwise shearing, unlike the former two. In this figure, $exp\left(\frac{-jk}{2d_3}x_i^2\right)$ cancels the previous two steps of modulation, and the spectrum returns to its original position.

When

$$\frac{jk}{2}\left(\frac{x_o^2}{d_1}+\frac{x_i^2}{d_2}-\frac{x_i^2}{d_3}\right)=0 \tag{26}$$

is satisfied, where $x_o=\frac{-d_1}{d_2}x_i$, that is

$$d_3=\frac{{d_2}^2}{d_1+d_2} \tag{27}$$

the distance between the lens and the CMOS target plane is

$$d_2 - d_3 = d_2 - \frac{{d_2}^2}{d_1 + d_2} = \frac{d_1 d_2}{d_1 + d_2} \tag{28}$$

According to Eq.(23), we have

$$f = \frac{d_1 d_2}{d_1 + d_2} \tag{29}$$

and the following formula:

$$d_4 = d_2 - d_3 = f \tag{30}$$

That is, when the distance between the lens and CMOS chip is the focal length of the lens, the holographic imaging process will not produce a new space-variance effect. Besides, it's necessary to exclude the influence of lens as much as possible since our focus is on the space-variance effect in digital holography. A large aperture lens can be used to ensure this. For example, in our experiment, a lens with a diameter of 50.8 mm is used as the image lens, thus satisfying the approximate space-invariance state. When the space-variance effect of imaging lens can be ignored, the whole holographic imaging system remains space invariant. From the perspective of Fourier optics, the back focal plane of the imaging lens is the Fourier plane of the object field; thus, the aperture stop located in the back focal plane is equivalent to the ideal low-pass filtering of the object field, so the imaging process is space invariant. In addition, for different object distances of the same imaging lens, its Fourier plane remains the same, so the recording position of focal plane holography also remains the same.

The prediction is verified by the simulations and experiments involving microlens array topography measurement. As shown in Fig. 10, an ordinary Mach–Zehnder interferometer is used for the experiment. A laser beam with a wavelength of 523.5 nm is used in our experiment, the focal length of the imaging lens is 200 mm, and the sample is placed 400 mm in front of the imaging lens to maintain a vertical axis magnification of 1×. The tested object is a lbtek MLAS10-F15-P300-AB microlens array with a period of 300 μm and window size of 9 mm × 9 mm. A CMOS camera with a resolution of 5120 × 5120 and pixel size of 2.5 μm is used for recording. To better compare the image quality of the three holography recording methods, the holograms are cropped to a resolution of 3800 × 3800 with a physical size of 9.5 mm.

For comparison, the following three sets of simulations and experiments are performed: Fresnel holography, image holography *with* recording holograms at the back focal plane (IHWF) and *without* recording holograms at the back focal plane of the imaging lens (IHWOF). To maintain the same numerical aperture as that in IHWF, the CMOS is placed 200 mm behind the sample in Fresnel holography and 200 mm behind the image plane of the imaging lens in IHWOF.

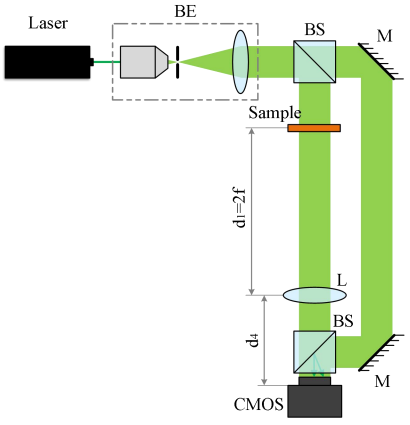

Fig.10. Schematic of the image holography. BE, beam expander with spatial filter; BS, beam splitter; M, plane mirror; L, imaging lens; d_1, object distance; d_4, distance between lens and CMOS; f, focal length of the lens L.

The simulation processes of Fresnel holography and image holography are based on the block diagrams shown in Fig. 2 and Fig. 8, and the simulation results under the above conditions are shown in Fig. 11 and Fig. 12 , respectively.

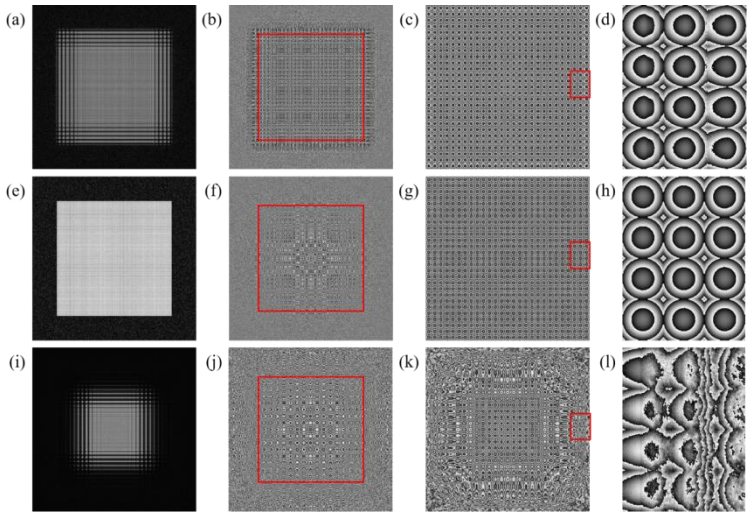

Fig. 11 (a–d), (e–h), and (i–l) are the simulation results of microlens array measurements obtained using Fresnel holography, IHWF, and IHWOF, respectively. (a), (e), and (i) are the intensity maps. (b), (f), and (j) are the wrapped phase maps; (c) is the enlarged image of the area in the red box in (b); and (g) and (k) are the wrapped phase maps after compensating for the phase aberration of the area in the red boxes in (f) and (j), respectively. (d), (h), and (l) are the enlarged images in the red boxes in (c), (g), and (k), respectively.

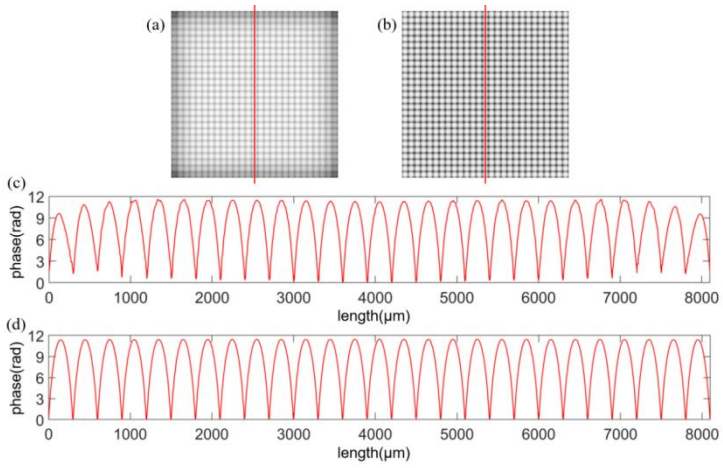

Fig. 12 Simulation results. (a) and (b) show the unwrapped phase maps of Fresnel holography and IHWF reconstructed wave front, respectively. (unwrapped results of the phase maps in Fig.11(c) and Fig.11(g), respectively) (c) and (d) represent the profile curves at the red line in (a) and (b), respectively.

Recording the hologram directly at the back focal plane of the imaging lens in the IHWF experiment is difficult because the energy of the zero-frequency component is too concentrated, and the overexposure of the low-frequency information is severe. Therefore, the CMOS target plane can slightly deviate from the focal plane to record the hologram and still maintain the approximate space invariant.

The experimental results are shown in Fig. 13 and Fig. 14. A discussion of the experimental results in Fig. 14 is necessary. In Fig. 14(c), because of the space-variance effect, the high-frequency information at the edge of the microlens array is lost. In addition, because

of the large gradient, the root of each microlens corresponds to the high-frequency information. Therefore, the closer the microlens is to the edge, the more serious the phase information is lost at the root, causing the phase at the root of these microlenses to be disturbed, while the phase in Fig. 14(d) is in order, which is exactly what we expect to observe.

Besides, there is a phenomenon of "phase increase" at the edge in Fig. 14, which may result from phase aberration. The experimental results in [35-41] indicate that in digital holographic phase measurement, it is difficult to perfectly control or eliminate the phase aberration in the whole field of view. However, the "phase increase" in Fig. 14 does not affect any of the analysis and conclusions of this article.

The simulation and the experimental results reveal that the imaging quality of IHWF is significantly higher than that of Fresnel holography and IHWOF and the imaging quality of IHWOF is worse than that of Fresnel holography. The latter can easily be explained by Figs. 8 and 9. For example, the bandwidth of the LFM signal in IHWOF is twice that of the LFM signal in Fresnel holography, so only the area in the center, which occupies approximately 1/4 of the total area in Fig. 11(k) and Fig. 13(k), has relatively high imaging quality. These results indicate that IHWF has the potential to suppress or even eliminate the space-variance effect and further indicate the correctness of the proposed theory.

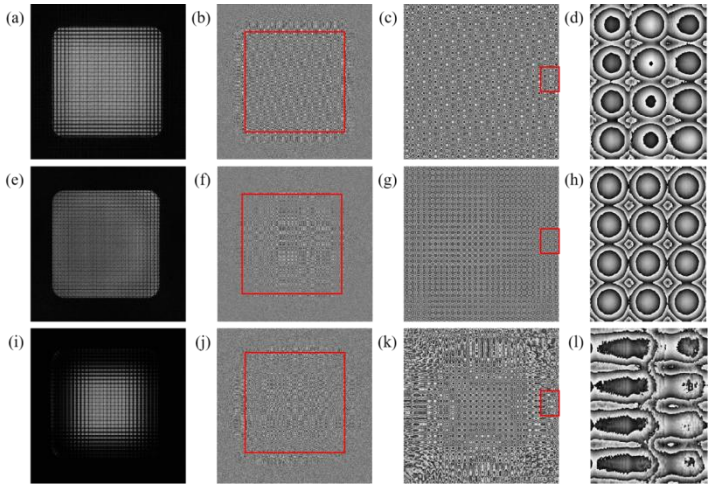

Fig. 13 (a–d), (e–h) and (i–l) are the experimental results of microlens array measurements for Fresnel holography, IHWF, and IHWOF, respectively. (a), (e) and (i) are the intensity maps. (b), (f), and (j) are the wrapped phase maps; (c) is the enlarged image of the area in the red box in (b); and (g) and (k) are the wrapped phase maps after compensating for the phase aberration of the area in the red boxes in (f) and (j), respectively. (d), (h), and (l) are the enlarged images in the red boxes in (c), (g), and (k), respectively.

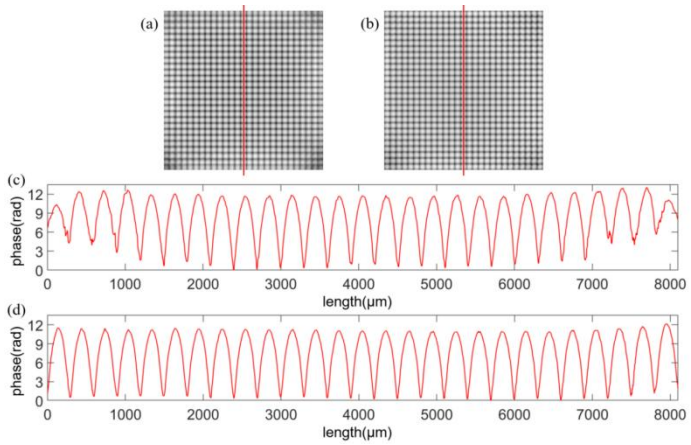

Fig. 14 Experimental results. (a) and (b) show the unwrapped phase maps of Fresnel holography and IHWF reconstructed wave front, respectively. (unwrapped results of the phase maps in Fig. 13(c) and Fig. 13(g), respectively) (c) and (d) are the profile curves at the red line in (a) and (b), respectively.

5. Conclusions

In this study, the digital holography imaging system is regarded as a space-variant system. In digital Fresnel holography, the space-variance effect severely affects the measurement results due to the small size of the CMOS chip. Therefore, it is inappropriate to treat it as a space-invariant system. The discussion of space-variance effects in Sections 2 and 3 of this paper is based on Fresnel holography, but it is also applicable to ordinary optical imaging systems. The presented analysis reveals that the space-variance effect is caused by LFM and ideal low-pass filtering. If one of these two conditions is destroyed, the space-variance effect can be eliminated. Furthermore, three states of the space-variance effect are pointed out: approximate space-invariance state, high-frequency distortion state, and boundary-diffraction state. In this study, the two physical phenomena of high-frequency distortion and boundary-diffraction are added to classical Fourier optical analysis of an optical imaging system which only considers the approximate space invariance state, making it more consistent with the fact.

Based on the theory proposed in this study, we have proved through theoretical analysis, simulation, and experiment that the space-variance effect can be controlled by adjusting the distance between the optical elements in the imaging system, especially when recording the hologram in back focal plane of the imaging lens, the holographic imaging process will not produce a new space-variance effect. In other words, when the space-variance effect of the imaging lens can be ignored, there will be no space-variance effect in the imaging system. Thus, this article provides a comprehensive understanding to digital holographic imaging system with space-variance effect.

Funding. National Natural Science Foundation of China (No.52175516); Youth Innovation Promotion Association, CAS (2022410).

References

1. J. W. Goodman, Introduction to Fourier optics, Fourth edition. ed. (W.H. Freeman, New York, 2017).
2. H. Yan, C. Y. Liu, L. Jun, C. Ping, K. M. Qian, and A. Asundi, "Investigation of the systematic axial measurement error caused by the space variance effect in digital holography," Opt. Lasers Eng. **112**, 16-25 (2019).
3. A. W. Lohmann and D. P. Paris, "SPACE-VARIANT IMAGE FORMATION," Journal of the Optical Society of America **55**, 1007-& (1965).
4. E. Brainis, C. Muldoon, L. Brandt, and A. Kuhn, "Coherent imaging of extended objects," Opt. Commun. **282**, 465-472 (2009).

5. D. A. Tichenor and J. W. Goodman, "COHERENT TRANSFER-FUNCTION," Journal of the Optical Society of America **62**, 293-& (1972).
6. A. Pan, C. Zuo, Y. G. Xie, M. Lei, and B. L. Yao, "Vignetting effect in Fourier ptychographic microscopy," Opt. Lasers Eng. **120**, 40-48 (2019).
7. F. Merola, P. Memmolo, L. Miccio, R. Savoia, M. Mugnano, A. Fontana, G. D'Ippolito, A. Sardo, A. Iolascon, A. Gambale, and P. Ferraro, "Tomographic flow cytometry by digital holography," Light-Sci. Appl. **6**, 7 (2017).
8. P. Girshovitz and N. T. Shaked, "Fast phase processing in off-axis holography using multiplexing with complex encoding and live-cell fluctuation map calculation in real-time," Opt. Express **23**, 8773-8787 (2015).
9. T. Tahara, X. Y. Quan, R. Otani, Y. Takaki, and O. Matoba, "Digital holography and its multidimensional imaging applications: a review," Microscopy **67**, 55-67 (2018).
10. J. Katz and J. Sheng, "Applications of Holography in Fluid Mechanics and Particle Dynamics," Annu. Rev. Fluid Mech. **42**, 531-555 (2010).
11. Y. Chen, D. R. Guildenbecher, K. N. G. Hoffmeister, M. A. Cooper, H. L. Stauffacher, M. S. Oliver, and E. B. Washburn, "Study of aluminum particle combustion in solid propellant plumes using digital in-line holography and imaging pyrometry," Combust. Flame **182**, 225-237 (2017).
12. L. Miccio, P. Memmolo, F. Merola, S. Fusco, V. Embrione, A. Paciello, M. Ventre, P. A. Netti, and P. Ferraro, "Particle tracking by full-field complex wavefront subtraction in digital holography microscopy," Lab Chip **14**, 1129-1134 (2014).
13. J. Kuhn, F. Charriere, T. Colomb, E. Cuche, F. Montfort, Y. Emery, P. Marquet, and C. Depeursinge, "Axial sub-nanometer accuracy in digital holographic microscopy," Meas. Sci. Technol. **19**, 8 (2008).
14. M. Agour, C. Falldorf, and R. B. Bergmann, "Spatial multiplexing and autofocus in holographic contouring for inspection of micro-parts," Opt. Express **26**, 28576-28588 (2018).
15. A. Khmaladze, A. Restrepo-Martinez, M. Kim, R. Castaneda, and A. Blandon, "Simultaneous dual-wavelength reflection digital holography applied to the study of the porous coal samples," Appl. Optics **47**, 3203-3210 (2008).
16. J. Kostencka, T. Kozacki, A. Kus, B. Kemper, and M. Kujawinska, "Holographic tomography with scanning of illumination: space-domain reconstruction for spatially invariant accuracy," Biomed. Opt. Express **7**, 4086-4101 (2016).
17. V. Balasubramani, A. Kus, H. Y. Tu, C. J. Cheng, M. Baczewska, W. Krauze, and M. Kujawinska, "Holographic tomography: techniques and biomedical applications Invited," Appl. Optics **60**, B65-B80 (2021).
18. C. J. Mann, L. F. Yu, C. M. Lo, and M. K. Kim, "High-resolution quantitative phase-contrast microscopy by digital holography," Opt. Express **13**, 8693-8698 (2005).
19. M. Yamagiwa, T. Minamikawa, C. Trovato, T. Ogawa, D. G. A. Ibrahim, Y. Kawahito, R. Oe, K. Shibuya, T. Mizuno, E. Abraham, Y. Mizutani, T. Iwata, H. Yamamoto, K. Minoshima, and T. Yasui, "Multicascade-linked synthetic wavelength digital holography using an optical- comb-referenced frequency synthesizer," Opt. Express **26**, 26292-26306 (2018).
20. E. Cuche, F. Bevilacqua, and C. Depeursinge, "Digital holography for quantitative phase-contrast imaging," Opt. Lett. **24**, 291-293 (1999).
21. S. K. Mohammed, L. Bouamama, D. Bahloul, and P. Picart, "Quality assessment of refocus criteria for particle imaging in digital off-axis holography," Appl. Optics **56**, F158-F166 (2017).
22. E. Cuche, P. Marquet, and C. Depeursinge, "Simultaneous amplitude-contrast and quantitative phase-contrast microscopy by numerical reconstruction of Fresnel off-axis holograms," Appl. Optics **38**, 6994-7001 (1999).
23. T. Colomb, E. Cuche, F. Charriere, J. Kuhn, N. Aspert, F. Montfort, P. Marquet, and C. Depeursinge, "Automatic procedure for aberration compensation in digital holographic microscopy and applications to specimen shape compensation," Appl. Optics **45**, 851-863 (2006).
24. E. Hecht, Optics, Global, fifth edition. ed. (Pearson, Boston, 2017).
25. A. Stein and G. Barbastathis, "Axial imaging necessitates loss of lateral shift invariance," Appl. Optics **41**, 6055-6061 (2002).
26. S. B. Oh and G. Barbastathis, "Axial imaging necessitates loss of lateral shift invariance: proof with the Wigner analysis," Appl. Optics **48**, 5881-5888 (2009).
27. M. M. Bastiaans, "Application of the Wigner distribution function in optics," in 1997),
28. R. C. Gonzalez and R. E. Woods, Digital image processing (Pearson, New York, NY, 2018), pp. xvi, 1168 pages.
29. T. Colomb, F. Montfort, J. Kuhn, N. Aspert, E. Cuche, A. Marian, F. Charriere, S. Bourquin, P. Marquet, and C. Depeursinge, "Numerical parametric lens for shifting, magnification, and complete aberration compensation in digital holographic microscopy," J. Opt. Soc. Am. A-Opt. Image Sci. Vis. **23**, 3177-3190 (2006).
30. C. Zuo, Q. Chen, W. J. Qu, and A. Asundi, "Phase aberration compensation in digital holographic microscopy based on principal component analysis," Opt. Lett. **38**, 1724-1726 (2013).
31. J. C. Curlander and R. N. McDonough, Synthetic aperture radar : systems and signal processing, Wiley series in remote sensing (John Wiley & Sons, Inc, New York, 1991), pp. xvii, 647 pages : illustrations.
32. W. Joseph, "Introduction To Fourier Optics 3rd Edition 2007 Joseph W," in 2021),

33. E. Cuche, P. Marquet, and C. Depeursinge, "Aperture apodization using cubic spline interpolation: application in digital holographic microscopy," Opt. Commun. **182**, 59-69 (2000).
34. J. Kuhn, B. Niraula, K. Liewer, J. K. Wallace, E. Serabyn, E. Graff, C. Lindensmith, and J. L. Nadeau, "A Mach-Zender digital holographic microscope with sub-micrometer resolution for imaging and tracking of marine micro-organisms," Rev. Sci. Instrum. **85**, 6 (2014).
35. X. Fan, J. J. Healy, K. O'Dwyer, J. Winnik, and B. M. Hennelly, "Adaptation of the Standard Off-Axis Digital Holographic Microscope to Achieve Variable Magnification," Photonics-Basel **8**(2021).
36. Z. Zhong, H. J. Zhao, M. G. Shan, B. Liu, W. L. Lu, and Y. B. Zhang, "Off-axis digital holographic microscopy with divided aperture," Opt. Lasers Eng. **127**(2020).
37. C. Zheng, D. Jin, Y. P. He, H. T. Lin, J. J. Hu, Z. Yaqoob, P. T. C. So, and R. J. Zhou, "High spatial and temporal resolution synthetic aperture phase microscopy," Adv Photonics **2**(2020).
38. B. C. Liu, D. Q. Feng, F. Feng, A. L. Tian, and W. G. Liu, "Maximum a posteriori-based digital holographic microscopy for high-resolution phase reconstruction of a micro-lens array," Opt. Commun. **477**(2020).
39. Z. B. Ren, J. L. Zhao, and E. Y. Lam, "Automatic compensation of phase aberrations in digital holographic microscopy based on sparse optimization," Apl Photonics **4**(2019).
40. X. L. Zhang, X. C. Zhang, M. Xu, H. Zhang, and X. Q. Jiang, "Phase unwrapping in digital holography based on non-subsampled contourlet transform," Opt. Commun. **407**, 367-374 (2018).
41. Y. F. Wen, W. J. Qu, H. B. Cheng, H. Yan, and A. Asundi, "Further investigation on the phase stitching and system errors in digital holography," Appl. Optics **54**, 266-276 (2015).